Geophysical Research Letters

RESEARCH LETTER
10.1029/2024GL112484

Key Points:

- We present observations made by the Blackstone SuperDARN radar, a Digisonde, and SAMI3 simulations to analyze the eclipsed ionosphere
- SuperDARN Doppler velocities cohered into a pattern clearly organized by the line of totality with a reversal in sign across the line
- SuperDARN skip distance and Digisonde derived foF2 show a delayed response to the shadow, suggesting slower response at higher altitudes

Correspondence to:
B. S. R. Kunduri,
bharatr@vt.edu

Citation:
Kunduri, B. S. R., Baker, J. B. H., Ruohoniemi, J. M., Thomas, E. G., Huba, J. D., Emmons, D. J., et al. (2024). HF radar observations and modeling of the impact of the 8 April 2024 total solar eclipse on the ionosphere-thermosphere system. *Geophysical Research Letters*, *51*, e2024GL112484. https://doi.org/10.1029/2024GL112484

Received 11 SEP 2024
Accepted 24 OCT 2024

Author Contributions:
Conceptualization: J. B. H. Baker, J. M. Ruohoniemi, E. G. Thomas, D. J. Emmons, A. T. Chartier
Data curation: J. B. H. Baker, J. M. Ruohoniemi, K. T. Sterne, G. Farinas Perez, W. A. Bristow, J. M. Holmes, E. V. Dao
Formal analysis: J. B. H. Baker, J. M. Ruohoniemi, E. G. Thomas, J. D. Huba, D. J. Emmons, D. R. Themens, S. G. Shepherd
Funding acquisition: J. B. H. Baker, J. M. Ruohoniemi, D. J. Emmons, A. T. Chartier, G. W. Perry
Investigation: J. B. H. Baker, J. M. Ruohoniemi, D. J. Emmons, W. A. Bristow, S. G. Shepherd
Methodology: J. B. H. Baker, J. M. Ruohoniemi, E. G. Thomas,

HF Radar Observations and Modeling of the Impact of the 8 April 2024 Total Solar Eclipse on the Ionosphere-Thermosphere System

B. S. R. Kunduri[1], J. B. H. Baker[1], J. M. Ruohoniemi[1], E. G. Thomas[2], J. D. Huba[3], D. J. Emmons[4], D. R. Themens[5], K. T. Sterne[1], G. Farinas Perez[1], W. A. Bristow[6], S. G. Shepherd[2], J. M. Holmes[7], E. V. Dao[7], A. T. Chartier[8], G. W. Perry[9], and K. Pandey[9]

[1]Bradley Department of Electrical and Computer Engineering, Blacksburg, VA, USA, [2]Thayer School of Engineering, Dartmouth College, Hanover, NH, USA, [3]Syntek Technologies, Fairfax, VA, USA, [4]Department of Engineering Physics, Air Force Institute of Technology, Wright-Patterson AFB, OH, USA, [5]School of Engineering, SERENE, University of Birmingham, Birmingham, UK, [6]Pennsylvania State University, University Park, PA, USA, [7]Space Vehicles Directorate, Air Force Research Laboratory, Kirtland AFB, NM, USA, [8]Johns Hopkins Applied Physics Lab, Laurel, MD, USA, [9]Center for Solar-Terrestrial Research, New Jersey Institute of Technology, Newark, NJ, USA

Abstract The path of totality of the 8 April 2024 solar eclipse traversed the fields-of-view of four US SuperDARN radars. This rare scenario provided an excellent opportunity to monitor the large-scale ionospheric response to the eclipse. In this study, we present observations made by the Blackstone (BKS) SuperDARN radar and a Digisonde during the eclipse. Two striking effects were observed by the BKS radar: (a) the Doppler velocities associated with ground scatter coalesced into a pattern clearly organized by the line of totality, with a reversal in sign across this line, and, (b) a delay of ∼45 min between time of maximum obscuration and maximum effect on the skip distance. The skip distance estimated using a SAMI3 simulation of the eclipse did not however capture the asymmetric time-delay. These observations suggest that the neutral atmosphere plays an important role in controlling ionospheric plasma dynamics, which were missing in SAMI3 simulations.

Plain Language Summary The total solar eclipse on 8 April 2024 was the last one to be observed over the continental United States until 2045. In addition to blocking the visible light from the Sun over a swath ranging a few hundred kilometers, a solar eclipse will also partially obscure the Sun's extreme ultraviolet radiation. As a result, an eclipse can drive significant changes in the ionosphere, a charged region in the Earth's upper atmosphere that is predominantly ionized by solar radiation. A unique feature of this eclipse was that the path of totality traversed the fields-of-view of three Super Dual Auroral Radar Network (SuperDARN) radars–Fort Hays East, Blackstone, and Wallops Island. SuperDARN radars operate in the High Frequency (HF) range, and radio waves in this frequency range are particularly sensitive to changes in the ionosphere. In this study, we use observations provided by SuperDARN radars alongside a Digisonde to determine the temporal response of the different ionospheric layers to the eclipse and compare these observations with modeled behavior.

1. Introduction

A total solar eclipse was observed over the continental United States on 8 April 2024. The path of totality began over the North Pacific Ocean near Mexico and traversed across several US states from Texas to Maine. A key feature of this solar eclipse is that the path of totality passed through large geographical sectors covered by the fields-of-view of three SuperDARN radars–namely, Fort Hays East (FHE), Blackstone (BKS), and Wallops Island (WAL). A coordinated observational campaign was conducted by researchers at Virginia Tech, Air Force Institute of Technology, Dartmouth College, and the Johns Hopkins Applied Physics Lab to make measurements of the ionosphere-thermosphere system during the eclipse. A key component of this campaign was to temporarily deploy a Digisonde at the Wright-Patterson Air Force Base (WP-AFB), which is located in the fields-of-view of two SuperDARN radars (BKS and FHE), and also along the path of totality.

A solar eclipse partially occults the Sun's extreme ultraviolet radiation coming from the extended corona and provides an environment analogous to a "controlled" experiment, allowing for an assessment of the response of the ionosphere's vertical plasma density structure to a sudden change in incident radiation. Several observational (Adeniyi et al., 2007; Coster et al., 2017; Jose et al., 2020; Yau et al., 2018; Zhang et al., 2017) and modeling

J. D. Huba, D. J. Emmons, D. R. Themens, W. A. Bristow, S. G. Shepherd
Project administration: J. B. H. Baker, J. M. Ruohoniemi
Resources: J. B. H. Baker, J. M. Ruohoniemi, J. D. Huba, D. J. Emmons, D. R. Themens, K. T. Sterne, G. Farinas Perez, W. A. Bristow, J. M. Holmes, E. V. Dao
Software: K. T. Sterne, G. Farinas Perez, W. A. Bristow, J. M. Holmes, E. V. Dao
Supervision: J. B. H. Baker, J. M. Ruohoniemi
Validation: J. B. H. Baker, J. M. Ruohoniemi
Visualization: J. B. H. Baker, J. M. Ruohoniemi
Writing – original draft: J. B. H. Baker, J. M. Ruohoniemi, J. D. Huba
Writing – review & editing: J. B. H. Baker, J. M. Ruohoniemi, E. G. Thomas, J. D. Huba, D. R. Themens, K. T. Sterne, W. A. Bristow, S. G. Shepherd, A. T. Chartier, G. W. Perry, K. Pandey

(Adeniyi et al., 2009; Cnossen et al., 2019; Müller-Wodarg et al., 1998; Rishbeth, 1968; Wang et al., 2019) studies examining previous eclipses have provided insights on the impact of eclipses on the ionosphere-thermosphere system. These studies focused on monitoring the variations in ionospheric plasma density structure during an eclipse and noted that peak change in plasma densities can lag the peak eclipse obscuration level, variously reported as a delay of ∼15 (Coster et al., 2017) or ∼80 min (Jose et al., 2020). The relatively localized and swift changes in solar radiation during an eclipse can generate a complex and asymmetric response in the upper atmosphere especially in the F-region and above (Adeniyi et al., 2007; Cnossen et al., 2019; Harding et al., 2018; Rishbeth, 1968; Zhang et al., 2017). Plasma densities at the lower altitudes that is, below the F-region, are expected to be predominantly controlled by photochemistry and therefore to directly correlate with eclipse induced changes in solar EUV radiation (Adeniyi et al., 2009; Rishbeth, 1968). At higher altitudes, especially in the F2 region, transport processes, ambipolar diffusion, and neutral composition are also expected to play important roles in determining ionospheric variability (Wang et al., 2019). Physics-based modeling by Cnossen et al. (2019) showed that the response of the neutral temperature lagged behind totality by ∼35 min and that the neutral winds had a noticeable influence on the Total Electron Content (TEC) during the 2017 total solar eclipse. Wang et al. (2019) used the Thermosphere Ionosphere Electrodynamics General Circulation Model (TIE-GCM) to show that the Moon's shadow can drive disturbances in neutral winds along its path which can alter F2 region electron densities.

Radio waves in the High Frequency (HF) range (3–30 MHz) are particularly sensitive to changes in the ionosphere and have long been used to remotely sense the state of the ionosphere (Breit & Tuve, 1926; Bland et al., 2014, 2018). The impact of the total solar eclipse of 21 August 2017 on SuperDARN was demonstrated by Moses et al. (2021), who showed that ground scatter moved to farther ranges or vanished entirely based on the look direction of the beam. A companion paper by Thomas et al. (2024) present first multi-frequency SuperDARN observations made by the Christmas Valley SuperDARN radars during the annular eclipse that occurred over North America on 14 October 2023. In this study, we present observations made by the BKS SuperDARN radar and the WP-AFB Digisonde during the total solar eclipse of 8 April 2024. We compare these observations with simulations of HF propagation through the eclipse obtained with the SAMI3 (Sami3 is A Model of the Ionosphere) model (Huba & Liu, 2020) to analyze the impact of eclipse induced changes in solar radiation at different altitudes.

2. Data Sets and Models

2.1. SuperDARN

SuperDARN is an international network of HF radars which are used for continuously monitoring ionospheric space weather phenomena (Chisham et al., 2007; Nishitani et al., 2019). The radars use electronic beam steering to typically scan through a total of 16–24 beams in 1–2 min, covering ∼50° in azimuth. In this study, we analyze ground backscatter power (signal-to-noise ratio) and Doppler velocities observed during the eclipse, as well as an additional parameter called the "sky noise" which provides an estimate of the average noise level across all the range gates. The sky noise parameter can be used as a proxy for ionospheric density variations in the *D* and lower *E* regions because it detects changes in HF absorption or propagation conditions (Berngardt et al., 2018; Bland et al., 2018). Lastly, we analyze changes in "skip distance" which is the distance from the radar to the closest point where signals are reflected from the ground.

2.2. SAMI3 Model

SAMI3 (Sami3 is A Model of the Ionosphere) (Huba et al., 2008; Huba & Liu, 2020) is a physics-based model of the ionosphere, which is based on Sami2 (Huba et al., 2008). In this study, we use SAMI3 simulated ionospheric electron density profiles to model the impact of the eclipse on HF propagation using ray-tracing. SAMI3 nominally uses the EUVAC (Richards et al., 1994) model for solar radiation and the Richmond apex model for the magnetic field (Richmond, 1995). The neutral composition, temperature, and winds in SAMI3 during this run have been specified using Naval Research Lab Mass Spectrometer Incoherent Scatter Radar (NRLMSIS-00) (Picone et al., 2002) and Horizontal Wind Model (HWM14) empirical models (Drob et al., 2015). The high-latitude electric potential is specified by the Weimer (2005) model. The mask used in SAMI3 to obscure the solar EUV radiation is similar to the one described by Huba and Drob (2017).

2.3. Digisonde at the Wright Patterson Air Force Base

A Digisonde DPS-4D from the Air Force Research Laboratory Space Vehicles Directorate (AFRL/RV) was temporarily installed at the Wright Patterson Air Force Base (WP-AFB), Ohio to determine the changes in the bottom side ionosphere during the eclipse. WP-AFB lies along the path of totality and also within the fields-of view of the BKS (Beam 6) and the FHE (Beam 22) radars, so the Digisonde provides important ionospheric context for interpreting the radar observations. Ionograms recorded during the eclipse were manually scaled and the critical frequencies of the *E* and F1/F2 layers determined at a 2-min cadence.

2.4. Ray-Tracing Through SAMI3 Eclipsed Ionosphere

Ray-tracing has provided insights into the propagation of HF radio waves in the ionosphere (e.g., Bristow & Greenwald, 1995; de Larquier et al., 2013; Kunduri et al., 2022, and others). In this study, we use the ray-tracing model developed by de Larquier (2013) which relies on a two–dimensional formulation of Fermat's principle in the propagation plane (Coleman, 1998). The de Larquier (2013) model estimates the refractive index by ignoring the impact of magnetic field and collisions. As a result, this approach cannot account for the differences in the propagation of the *O* and *X* modes and the estimates of the location of ground and ionospheric scatter generated by the ray-tracing simulations can be offset by 1–3 range gates. SAMI3 (Huba et al., 2008) simulations of the eclipsed ionosphere are used to model BKS observations during the eclipse along beam 6 which overlooks the WP-AFB Digisonde.

3. Observations

The upper panel of Figure 1 highlights the favorable alignment of the path of totality for the 8 April 2024 solar eclipse with the fields of view of several US SuperDARN radars. The path of totality is marked by the gray shaded region and contours of 20%, 40%, 60%, and 80% obscurity levels at 300 km altitude are also overlaid. The blue cross indicates the location of WP-AFB where a temporary Digisonde was deployed as a part of the observational eclipse campaign. It can also be seen from the figure that beam-6 to beam-22 of the BKS and FHE radars are oriented to look directly over the location of the Digisonde. The lower panels show ray-tracing results through the SAMI3 eclipsed ionosphere for beam-6 of the BKS radar at 17:30 UT (pre-eclipse), 19:30 UT (near totality), and 20:30 UT (post totality), respectively. Each ray is plotted in pink and the length of a ray path to a scatter point is the slant range. Note, that at 17:30 UT (pre-totality) rays are expected to reach the ground between 700 km (skip distance) and 1,500 km producing ground scatter. During totality (19:30 UT), the ground range of the skip distance extends beyond 1,000 km because of the decrease in electron densities. Finally, post totality (20:30 UT), the skip distance returns back to pre-eclipse levels to ∼700 km once the ionosphere recovers. Overall, ray-tracing through SAMI3 ionosphere suggests that we would expect the skip distance to change by ∼400 km during the eclipse, with the maximum offset expected to occur near 19:30 UT. The model suggests a small delay between the maximum offset in skip-distance and peak obscuration which occurs at ∼19:15 UT.

We will now analyze observations made by the BKS radar during the eclipse. In Figure 2, we show the impact of the eclipse on the Doppler velocities of ground backscatter observed by the BKS radar at two different times. The left panel shows observations at 19:00 UT just before totality (marked by the pink cross) enters the field-of-view, and the right panel shows observations at 19:18 UT, when totality is inside the field-of-view. The background in each scan plot is gray-scale color-coded by the level of obscurity in visible radiation. Prior to the arrival of totality the velocities over the inner band that covers all beams are small (<10 m/s) and generally negative, consistent with either a rising height of reflection or a changing index of refraction in the lower ionosphere (weak and variable velocity is typical of day time ground-scatter which can be perturbed by traveling ionospheric disturbances or solar flares) (Davies, 1990).

There is a dramatic change in the ground scatter Doppler velocities (color-coded according to the color bar on the right) as totality crosses the field-of-view of the radar. Specifically, at 1900 UT, we notice an increase in the magnitude of negative Doppler velocities (dark red colors) to ∼−25 m/s in the zonal beams which are closest to totality. This shift is consistent with a increase in the refractive index or effective reflection height. At 1918 UT, there is a transition in the Zonal beams from negative to positive Doppler velocities (now reaching ∼20 m/s) as the shadow crosses these beams and the ionosphere begins to recover. The meridional beams which are encountering the ascending phase of the eclipse are experiencing a increase in refractive index or effective reflection height of the signal, and therefore observe higher negative velocities. The sudden intensification and organization of

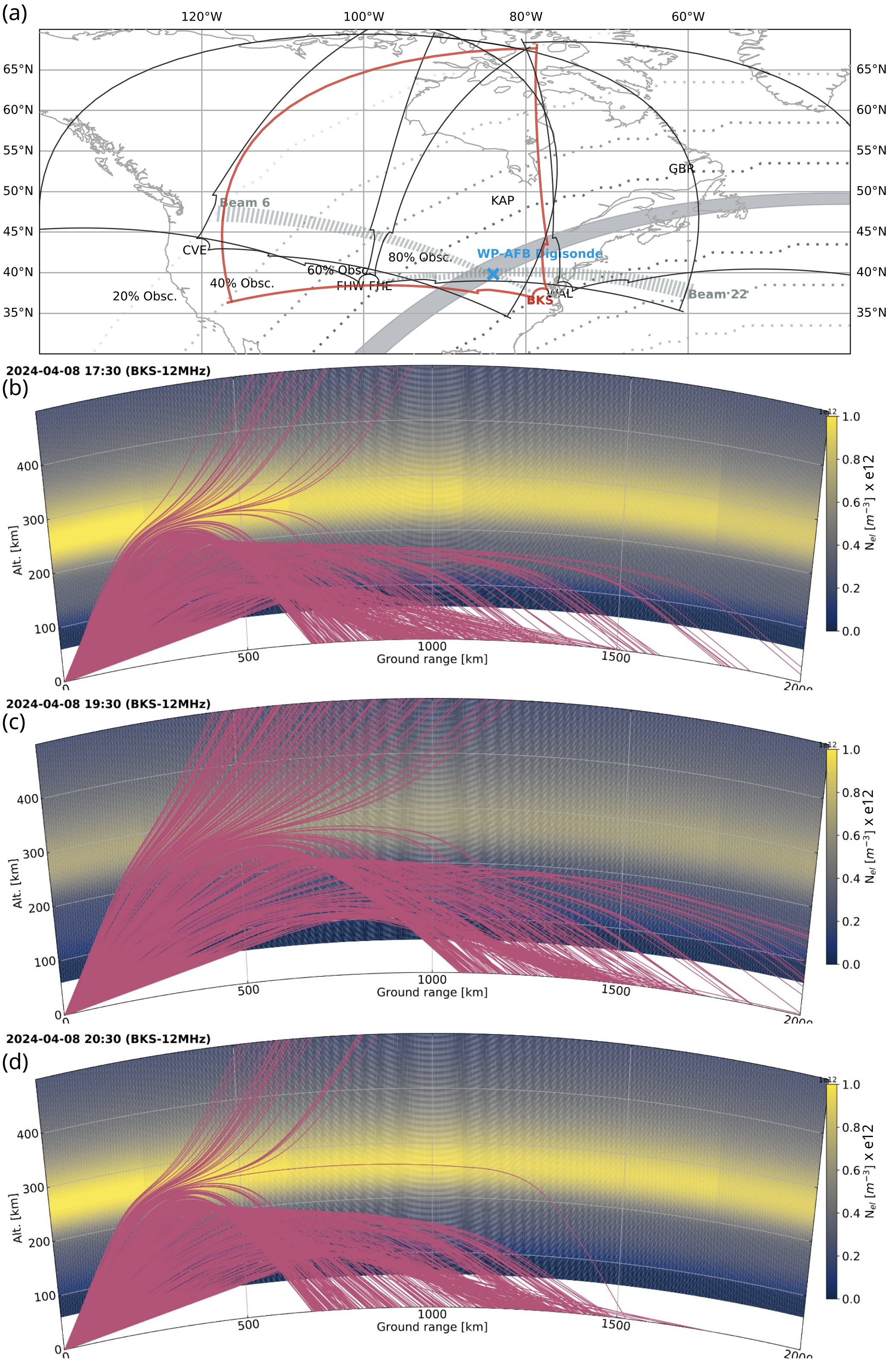
(a)
120°W
100°W
80°W
60°W
65°N
60°N
55°N
50°N
45°N
40°N
35°N
GBR
KAP
Beam 6
CVE
80% Obsc.
WP-AFB Digisonde
60% Obsc.
40% Obsc.
20% Obsc.
FHW FHE
BKS
WAL
Beam 22
2024-04-08 17:30 (BKS-12MHz)
(b)
2024-04-08 19:30 (BKS-12MHz)
(c)
2024-04-08 20:30 (BKS-12MHz)
(d)
Alt. [km]
100
200
300
400
0
500
1000
1500
2000
Ground range [km]
1e12
1.0
0.8
0.6
0.4
0.2
0.0
N_{el} [m^{-3}] x e12

Figure 1.

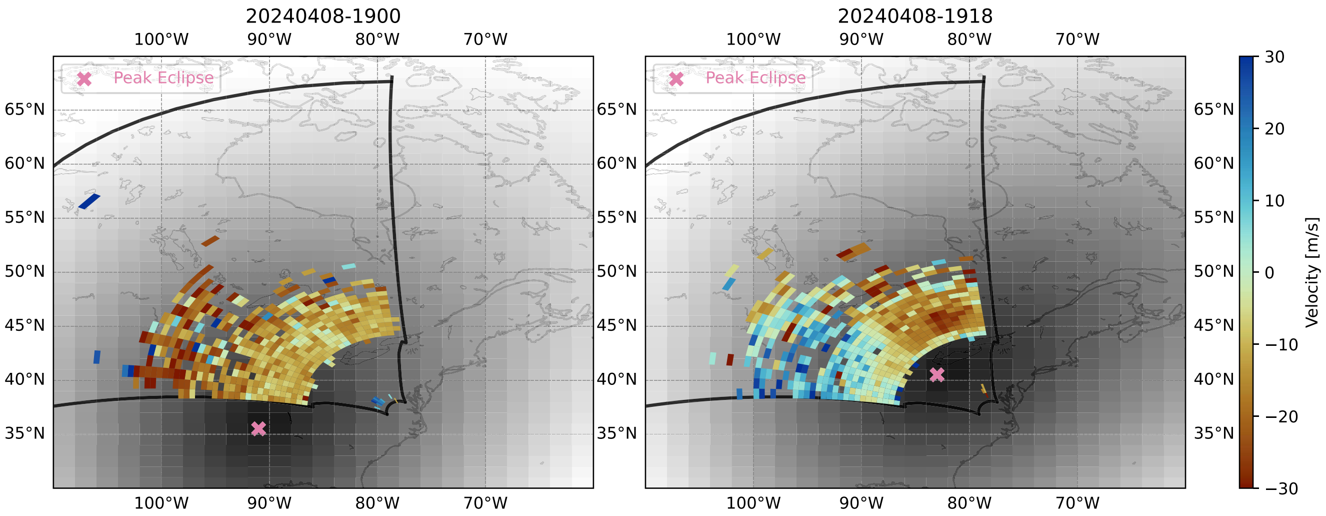

Figure 2. Fan-plots of color-coded Doppler velocities measured by the BKS radar at 1900 UT (left) prior to eclipse totality and 1918 UT (right) during the eclipse totality. The background is gray-scale color-coded by the level of obscurity with black being maximum. The totality location is identified by the pink cross.

Doppler velocities by the line of totality, defined as extending from the radar site to the "X-spot" and beyond is striking.

Figure 3 shows the temporal response in SuperDARN ground backscatter and sky noise to the intensity of the eclipse shadow. The top and bottom panels show Doppler velocities observed along beams 3 and 11 of the BKS radar. The gray-black contours indicate the level of maximum eclipse obscuration corresponding to blockage of the visible disk of the sun. The solar corona as a source of EUV increases the size of the disk that is effective on the ionosphere by approximately 15% (Mrak et al., 2018). Consideration of this factor would shift the start and end times of total obscuration by 5–10 min. Three important features can be observed. First, a remarkable alignment between the eclipse contours and the change in Doppler velocities is apparent. This alignment indicates that the shadow intensity is directly correlated to the change in Doppler velocity. Second, sky noise increases with increasing shadow intensity and vice versa. One possible reason for this behavior could be that HF attenuation decreased during the ascending phase of the eclipse and increased during recovery. Lastly, there is a delay in the response of skip distance to the eclipse contours such that the skip distance was observed to remain relatively constant as the intensity of obscuration increased, and started to increase only after the totality had passed through the field of view. A total delay of $\sim$45 min between the peak obscuration and the maximum offset in skip distance can be observed. The asymmetric response in the Doppler velocities/sky noise and the skip distance to the intensity of the eclipse shadow will be examined further.

Figure 4 shows a comparison between the ray-tracing simulations and actual observations along beam-6 of the BKS radar. Panel-(a) of Figure 4 presents relative sky noise across all beams as a function of UT time with the gray-black contours indicating peak eclipse obscurity levels along each beam. Relative sky noise is calculated by subtracting sky noise on the eclipse day (8 April) from a background level which is calculated using median values (binned by beam over a 30 min interval) from nearby days: 6^{th},7^{th},9^{th}, and 10^{th} April. This approach to estimate relative sky noise is similar to the one taken by Bland et al. (2018), however, the main difference is that they subtract median values of sky noise (binned by beam and frequency in 30 min intervals) from the previous 30 days. We limited our analysis to ±2 days because of a major upgrade to the BKS electronics in the last week of

Figure 1. The path of totality passed through the fields-of-view of four US mid-latitude SuperDARN radars: Christmas Valley East (CVE), Fort Hays East (FHE), Blackstone (BKS), and Wallops Island (WAL). The Fort Hays West (FHW) experienced lower levels of obscurity (<60%). The blue cross indicates the location of the Digisonde at the Wright Patterson Air Force Base (WP-AFB), and beams 22/6 from FHE/BKS radar that overlap the Digisonde are also marked in the figure. The lower three panels (b, c, and d) show Ray-tracing along beam-6 of the BKS radar through a SAMI3 eclipsed ionosphere at 17:30 UT prior to totality, 19:30 UT during totality, and 20:30 UT post totality. Electron densities are color coded according to the scale on the right and the pink lines represent rays between 5° and 50° elevation with 0.1° spacing. The simulations were performed at the same frequency at which the radar was operating during the eclipse (12 MHz).

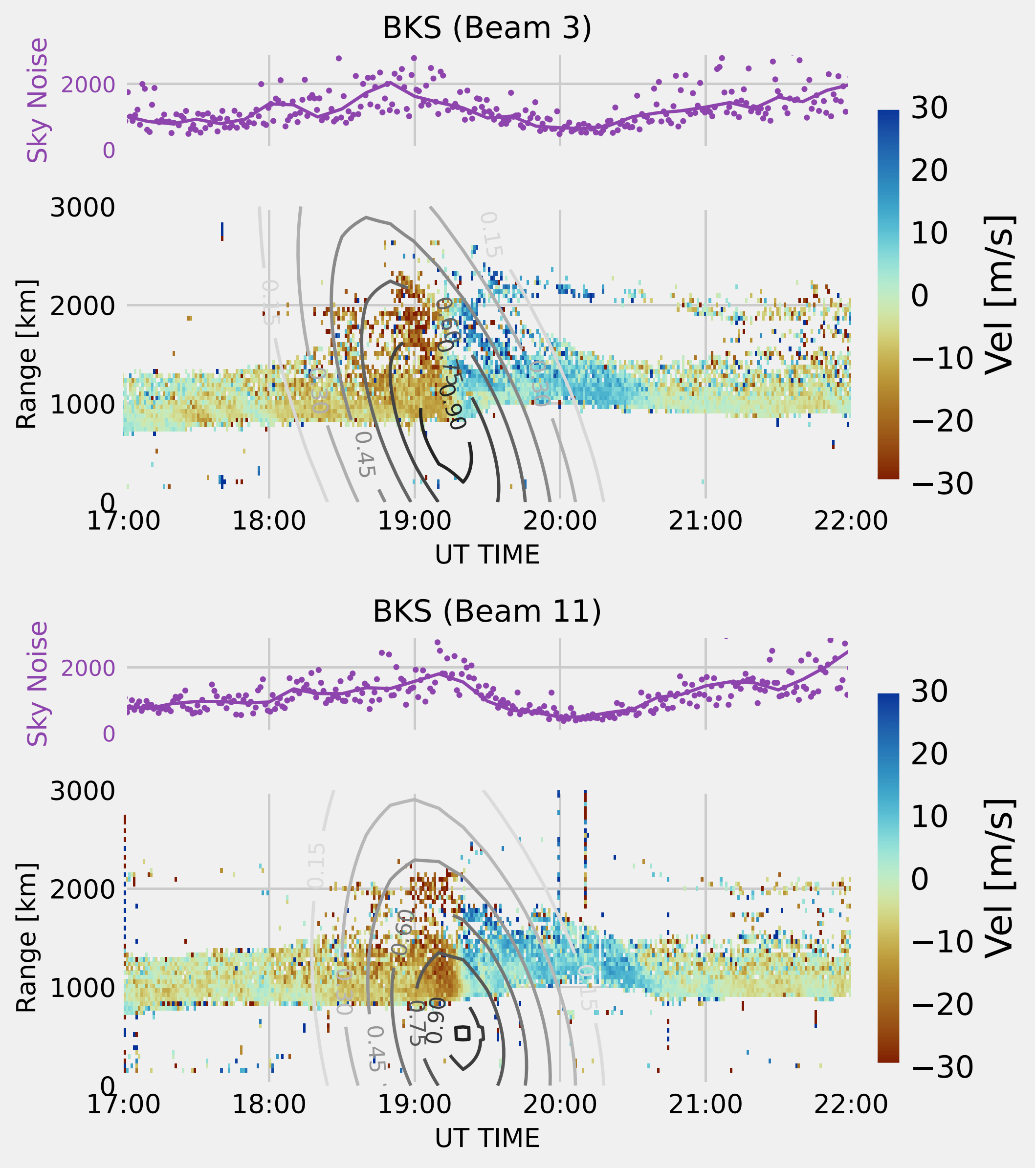

Figure 3. Sky noise level and Range-Time-Intensity (RTI) plot of color-coded Doppler velocities measured by the BKS radar along Beam-3 (top) and Beam-11 (bottom) between 17 and 22 UT. Overlaid as contours are the corresponding eclipse obscurity levels along the beam.

March 2024, to a new system based on the one designed by Bristow (2019). Similar to the observations presented in Figure 3, there is a direct correlation between sky noise and eclipse shadow intensity across all the beams.

In Figure 4b we present a direct comparison between the skip distance estimated using ray-tracing (Figure 1) and actual SuperDARN observations. Also overlaid is the SAMI3 derived foF2 at WP-AFB as pink dashes. It can be seen that the SAMI3 estimated skip distance is in reasonable agreement with actual BKS observations pre-eclipse (with a difference ranging between 100 and 200 km) and post-eclipse (difference <100 km), suggesting the model has captured important features of the background ionosphere well. However, there is a noticeable delayed response in the BKS-observed skip distance such that the maximum offset in observed skip distance occurs at 2000 UT, well past the time when maximum obscuration in eclipse shadow intensity is observed. The SAMI3 simulations on the other hand predict the maximum skip distance offset to occur at 1930 UT, only slightly behind maximum obscuration. This model-data offset in timing is further examined in panel-(c) where

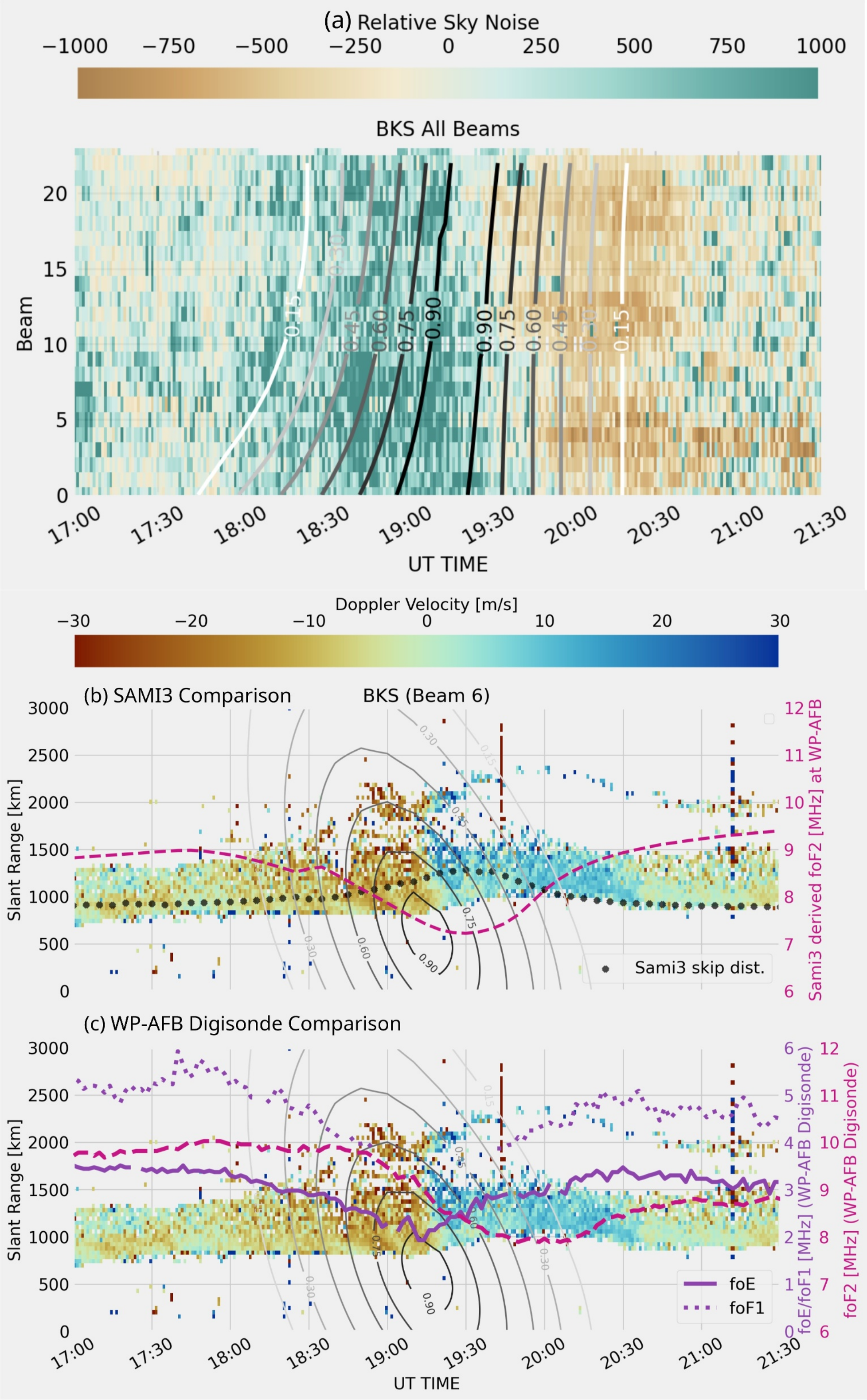

Figure 4. Panel-a (top) shows a time series plot of relative sky noise observed across all BKS beams. Overlaid as contours are the corresponding peak eclipse obscurity levels. Panels (b, c) show Range-Time-Intensity (RTI) plots of color-coded backscatter Doppler velocities along Beam-6 between 1700 and 2130 UT. In Panel (b), overlaid are the "skip-distance" estimated by raytracing through the SAMI3 eclipsed ionosphere and foF2 derived from Sami3 estimates at WP-AFB. In Panel (c), observations of foE, foF1, and foF2 made by the Digisonde deployed at WP-AFB are overlaid.

foF2 (pink dashed line), foF1 (purple dotted line), and foE (purple solid line) determined from the WP-AFB Digisonde are overlaid along with the same BKS Doppler velocities measured along beam-6. Two major features can be observed. First, WP-AFB foF2 drops to a minimum value of ∼8 MHz at 2000 UT, similar to the delay observed in BKS skip distance and changes in both the data sets are observed to be synchronized. Secondly, changes in foE and foF1 are well correlated with the intensity of the shadow of the eclipse and SuperDARN Doppler velocities.

4. Discussion and Summary

A prominent feature in Figure 2 through 4 is the response of the Doppler velocities to the eclipse shadow intensity. This behavior is consistent with observations presented in previous studies of solar flares (e.g., Kikuchi et al., 1986; Watanabe & Nishitani, 2013) and solar eclipses (e.g., Jakowski et al., 2008) which showed that changes in ground scatter Doppler velocity are correlated with the rate of electron density change in the bottomside ionosphere. In particular, we expect a decrease in the ionospheric electron densities and increase in refractive index as the eclipse approaches and vice-versa as the eclipse moves away. A change in the refractive index of the ionosphere can result in an apparent increase/decrease in the ray path and thereby produce the negative/positive Doppler velocity shift that is observed in Figure 2 through 4. A key question that needs to be addressed, however, is the relative contribution of the different layers (*D*, *E*, and *F*) to the Doppler velocity shift observed by the BKS radar. The variations in sky noise in Figures 3 and 4a indicate a likely reduction in HF absorption, due to a reduction in electron densities in the *D* and *E* regions (Berngardt et al., 2018; Bland et al., 2018), during the ascending phase of the eclipse and vice-versa. Taken together, the direct response of the Doppler velocities and sky noise to the changes in eclipse shadow intensity suggest that the lower ionosphere (the D- and E-regions) are responding relatively quickly to the eclipse. Indeed, the swift response of WP-AFB foE, along with a delayed response in foF2 and SuperDARN skip distance as shown in Figure 4c further confirm that the lower regions (D/E) are responding almost simultaneously to the eclipse shadow, whereas, the higher altitudes (F2 region) are showing a delayed response.

This leads us to an interesting question: What is causing the delay in the response of the F2 layer to the eclipse shadow? A delayed ionospheric response to the eclipse shadow was reported during previous eclipses using ionosondes (Adeniyi et al., 2007; Jose et al., 2020), and TEC observations (Coster et al., 2017; Zhang et al., 2017). The ∼30–60 min delay between the peak of the eclipse shadow and the maximum change in SuperDARN skip distance (Figures 3 and 4) is in reasonable agreement with a 45-min delay in the response of the F-region reported by Adeniyi et al. (2007) during the 29 March 2006 eclipse over an equatorial station, and a 60-min delay that was reported by Jose et al. (2020) near the Indian sector. Wang et al. (2019) used TIE-GCM to determine the relative contributions of different factors such as production and loss rates, ambipolar diffusion, neutral wind transport, etc., to electron density changes at different altitudes during the 2017 eclipse at Millstone Hill. They reported a delay of ∼30-min in the F-region which increased at higher altitudes. While photochemistry dominated lower altitudes (<200 km), the changes in density produced by transport of plasma from eclipse generated wind variations and ambipolar diffusion played an important role in controlling the dynamics at higher altitudes (Cnossen et al., 2019; Wang et al., 2019). Collectively, these results suggest that the contribution of the neutral atmosphere can vary greatly with factors such as local time, and location with respect to the eclipse path. Ionospheric response during an eclipse is also related to occultation in the extreme ultraviolet (EUV)/X-ray bands (Cantrall et al., 2024; Mrak et al., 2018). In particular, Mrak et al. (2018) used EUV occultation maps estimated from Solar Dynamics Observatory Atmospheric Imaging Assembly images to show that large-scale TEC disturbances observed during the great American eclipse of 21 August 2017 were produced by gradients in EUV illumination. Similarly, Mrak et al. (2022) developed a model of a solar eclipse mask at EUV wavelengths, and showed using Global Ionosphere Thermosphere Model (GITM) simulations that a modeled EUV eclipse mask can account for a 20% change in TEC, F-region plasma drift, and F-region neutral winds. A geometrically symmetric approximation of the occultation function may not fully express the impact of the eclipse shadow on the ionosphere-thermosphere system since the highly variable solar corona can make a notable contribution toward X-ray and EUV radiation. While the thermospheric response is likely the major contributor to the delay in the response of the F2 layer, an EUV mask (Mrak et al., 2022; Verhulst & Stankov, 2020) might also account for a portion of this delay. Multi-frequency experiments conducted with the CVE SuperDARN radar during the October 2023 annular solar eclipse were analyzed in the companion paper by Thomas et al. (2024). The authors report that skip distance was well correlated with the F_2-layer density response, which lags the peak obscuration by ∼30 min.

A better simulation of the 8 April 2024 eclipse is needed to fully understand the features of the ionosphere-thermosphere system. The discrepancy between the SAMI3 model estimates and observations seen in Figures 1 and 4 may be attributed to at least two factors. First, the SAMI3 results presented in this paper used the empirical models NRLMSIS-00 and HWM14 to define the thermospheric conditions; as such, they cannot capture the response of the neutral atmosphere to the eclipse (i.e., cooling, modified wind patterns). Second, the EUV mask used in SAMI3 is based on the ground location of the eclipse path. However, Verhulst and Stankov (2020) show that the three-dimensional geometry of solar eclipses needs to be considered, especially with regard to altitude. In fact, the path of the EUV masking of the central eclipse is height dependent and can affect the response of the ionosphere by 30–60 min (Verhulst & Stankov, 2020). These factors will be considered in future SAMI3 simulations. A comprehensive model-data comparison using observations made by multiple SuperDARN radars, covering different levels of obscurity, across the North American sector, will be the focus of a follow on study.

Overall, these observations demonstrate that the ionosphere-thermosphere system response to the eclipse is complex and the neutral atmosphere can play an important role in controlling the dynamics of ionospheric plasma density variability.

Data Availability Statement

Data underlying this manuscript are made accessible through the Virginia Tech Data Repository at Ruohoniemi et al. (2024). Eclipse obscuration levels were calculated using Frissell (2017).

Acknowledgments

We thank NASA for support under Grants 80NSSC23K1321 and 80NSSC22K1635 and the National Science Foundation for support under Grant AGS-1935110. This work acknowledges support by the NASA DRIVE Science Center for Geospace Storms under award 80NSSC22M0163. The research of JDH was supported by NASA Grant 80NSSC23K1322 and AFOSR Grant FA9550-22-C-0001. JMH and EVD were supported in part by the Air Force Office of Scientific Research (AFOSR), Grant 23RVCOR002. EGT and SGS acknowledge support from NSF under Grant AGS-1934997 and the Office of Naval Research under Grant N000142312109.

References

Adeniyi, J. O., Oladipo, O. A., Radicella, S. M., Adimula, I. A., & Olawepo, A. O. (2009). Analysis on 29 March 2006 eclipse effect on the ionosphere over Ilorin, Nigeria. *Journal of Geophysical Research*, *114*(A11). https://doi.org/10.1029/2009JA014416

Adeniyi, J. O., Radicella, S. M., Adimula, I. A., Willoughby, A. A., Oladipo, O. A., & Olawepo, O. (2007). Signature of the 29 March 2006 eclipse on the ionosphere over an equatorial station. *Journal of Geophysical Research*, *112*(A6). https://doi.org/10.1029/2006JA012197

Berngardt, O., Ruohoniemi, J., Nishitani, N., Shepherd, S., Bristow, W., & Miller, E. (2018). Attenuation of Decameter wavelength sky noise during x-ray solar flares in 2013–2017 based on the observations of Midlatitude hf radars. *Journal of Atmospheric and Solar-Terrestrial Physics*, *173*, 1–13. https://doi.org/10.1016/j.jastp.2018.03.022

Bland, E. C., Heino, E., Kosch, M. J., & Partamies, N. (2018). Superdarn radar-derived hf radio attenuation during the September 2017 solar proton events. *Space Weather*, *16*(10), 1455–1469. https://doi.org/10.1029/2018SW001916

Bland, E. C., McDonald, A. J., de Larquier, S., & Devlin, J. C. (2014). Determination of ionospheric parameters in real time using Superdarn hf radars. *Journal of Geophysical Research: Space Physics*, *119*(7), 5830–5846. https://doi.org/10.1002/2014JA020076

Breit, G., & Tuve, M. A. (1926). A test of the existence of the conducting layer. *Physics Reviews*, *28*(3), 554–575. https://doi.org/10.1103/PhysRev.28.554

Bristow, W. A. (2019). Application of radar imaging analysis to superdarn observations. *Radio Science*, *54*(7), 692–703. https://doi.org/10.1029/2019RS006851

Bristow, W. A., & Greenwald, R. A. (1995). Estimating gravity wave parameters from oblique high-frequency backscatter: Modeling and analysis. *Journal of Geophysical Research*, *100*(A3), 3639–3648. https://doi.org/10.1029/94JA02704

Cantrall, C. E., Mrak, S., Paxton, L. J., Zhang, Y., Nikoukar, R., Schaefer, R. K., & Yee, J. H. (2024). Source of the observed enhancements in thermospheric o/n2 during two solar eclipses in 2023. *Journal of Geophysical Research: Space Physics*, *129*(7), e2024JA032542. https://doi.org/10.1029/2024JA032542

Chisham, G., Lester, M., Milan, S., Freeman, M., Bristow, W., Grocott, A., et al. (2007). A decade of the Super Dual Auroral Radar Network (SuperDARN): Scientific achievements, new techniques and future directions. *Surveys in Geophysics*, *28*(1), 33–109. https://doi.org/10.1007/s10712-007-9017-8

Cnossen, I., Ridley, A. J., Goncharenko, L. P., & Harding, B. J. (2019). The response of the ionosphere-thermosphere system to the 21 August 2017 solar eclipse. *Journal of Geophysical Research: Space Physics*, *124*(8), 7341–7355. https://doi.org/10.1029/2018JA026402

Coleman, C. J. (1998). A ray tracing formulation and its application to some problems in over-the-horizon radar. *Radio Science*, *33*(4), 1187–1197. https://doi.org/10.1029/98RS01523

Coster, A. J., Goncharenko, L., Zhang, S.-R., Erickson, P. J., Rideout, W., & Vierinen, J. (2017). GNSS observations of ionospheric variations during the 21 August 2017 solar eclipse. *Geophysical Research Letters*, *44*(24), 12041–12048. https://doi.org/10.1002/2017GL075774

Davies, K. (1990). Ionospheric radio (No. 31). Iet.

de Larquier, S. (2013). The mid-latitude ionosphere under quiet geomagnetic conditions: Propagation analysis of SuperDARN radar observations for large ionospheric perturbations. *ProQuest Dissertations and Theses*, *126*.

de Larquier, S., Ponomarenko, P., Ribeiro, A. J., Ruohoniemi, J. M., Baker, J. B. H., Sterne, K. T., & Lester, M. (2013). On the spatial distribution of Decameter–scale subauroral ionospheric irregularities observed by SuperDARN radars. *Journal of Geophysical Research: Space Physics*, *118*(8), 5244–5254. https://doi.org/10.1002/jgra.50475

Drob, D. P., Emmert, J. T., Meriwether, J. W., Makela, J. J., Doornbos, E., Conde, M., et al. (2015). An update to the Horizontal Wind Model (HWM): The quiet time thermosphere. *Earth and Space Science*, *2*(7), 301–319. https://doi.org/10.1002/2014EA000089

Frissell, N. (2017). w2naf/eclipse_calculator v1.0. *Zenodo*. https://doi.org/10.5281/zenodo.1120440

Harding, B. J., Drob, D. P., Buriti, R. A., & Makela, J. J. (2018). Nightside detection of a large-scale thermospheric wave generated by a solar eclipse. *Geophysical Research Letters*, *45*(8), 3366–3373. https://doi.org/10.1002/2018GL077015

Huba, J. D., & Drob, D. (2017). SAMI3 prediction of the impact of the 21 August 2017 total solar eclipse on the ionosphere/Plasmasphere system. *Geophysical Research Letters*, *44*(12), 5928–5935. https://doi.org/10.1002/2017GL073549

Huba, J. D., Joyce, G., & Krall, J. (2008). Three-dimensional equatorial spread f modeling. *Geophysical Research Letters*, *35*(10). https://doi.org/10.1029/2008GL033509

Huba, J. D., & Liu, H.-L. (2020). Global modeling of equatorial spread f with Sami3/Waccm-x. *Geophysical Research Letters*, *47*(14), e2020GL088258. https://doi.org/10.1029/2020GL088258

Jakowski, N., Stankov, S., Wilken, V., Borries, C., Altadill, D., Chum, J., et al. (2008). Ionospheric behavior over Europe during the solar eclipse of 3 October 2005. *Journal of Atmospheric and Solar-Terrestrial Physics*, *70*(6), 836–853. https://doi.org/10.1016/j.jastp.2007.02.016

Jose, L., Vineeth, C., Pant, T. K., & Kumar, K. K. (2020). Response of the equatorial ionosphere to the annular solar eclipse of 15 January 2010. *Journal of Geophysical Research: Space Physics*, *125*(8), e2019JA027348. https://doi.org/10.1029/2019JA027348

Kikuchi, T., Sugiuchi, H., Ishimine, T., Maeno, H., & Honma, S. (1986). Solar-terrestrial disturbances of June-September 1982. iv. Ionospheric disturbances. xi. hf Doppler observations. Radio Research Laboratory. *The Journal*, *33*(1), 239–255.

Kunduri, B. S. R., Baker, J. B. H., Ruohoniemi, J. M., Thomas, E. G., & Shepherd, S. G. (2022). An examination of SuperDARN backscatter modes using machine learning guided by Ray-tracing. *Space Weather*, *20*(9), e2022SW003130. https://doi.org/10.1029/2022SW003130

Moses, M. L., Kordella, L. J., Earle, G. D., Drob, D., Huba, J. D., Ruohoniemi, J. M., et al. (2021). Observations and modeling studies of solar eclipse effects on oblique high frequency radio propagation. *Space Weather*, *19*(3). https://doi.org/10.1029/2020SW002560

Mrak, S., Semeter, J., Drob, D., & Huba, J. D. (2018). Direct Euv/x-ray modulation of the ionosphere during the August 2017 total solar eclipse. *Geophysical Research Letters*, *45*(9), 3820–3828. https://doi.org/10.1029/2017GL076771

Mrak, S., Zhu, Q., Deng, Y., Dammasch, I. E., Dominique, M., Hairston, M. R., et al. (2022). Modeling solar eclipses at extreme ultra violet wavelengths and the effects of nonuniform eclipse shadow on the ionosphere-thermosphere system. *Journal of Geophysical Research: Space Physics*, *127*(12), e2022JA031058. https://doi.org/10.1029/2022JA031058

Müller-Wodarg, I. C. F., Aylward, A. D., & Lockwood, M. (1998). Effects of a mid-latitude solar eclipse on the thermosphere and ionosphere—A modelling study. *Geophysical Research Letters*, *25*(20), 3787–3790. https://doi.org/10.1029/1998GL900045

Nishitani, N., Ruohoniemi, J. M., Lester, M., Baker, J. B. H., Koustov, A. V., Shepherd, S. G., et al. (2019). Review of the accomplishments of mid-latitude Super Dual Auroral Radar Network (SuperDARN) hf radars. *Progress in Earth and Planetary Science*, *6*(1), 1–57. https://doi.org/10.1186/s40645-019-0270-5

Picone, J. M., Hedin, A. E., Drob, D. P., & Aikin, A. C. (2002). Nrlmsise-00 empirical model of the atmosphere: Statistical comparisons and scientific issues. *Journal of Geophysical Research*, *107*(A12), 15–16. https://doi.org/10.1029/2002JA009430

Richards, P. G., Fennelly, J. A., & Torr, D. G. (1994). Euvac: A solar EUV flux model for aeronomic calculations. *Journal of Geophysical Research*, *99*(A5), 8981–8992. https://doi.org/10.1029/94JA00518

Richmond, A. D. (1995). Ionospheric electrodynamics using magnetic apex coordinates. *Journal of Geomagnetism and Geoelectricity*, *47*(2), 191–212. https://doi.org/10.5636/jgg.47.191

Rishbeth, H. (1968). Solar eclipses and ionospheric theory. *Space Science Reviews*, *8*(4), 543–554. https://doi.org/10.1007/BF00175006

Ruohoniemi, J. M., Baker, J. B., Kunduri, B. S. R., & Sterne, K. T. (2024). Blackstone SuperDARN and the Wright-Patterson Air Force Base Digisonde observations during the April 8, 2024 Eclipse [Dataset]. *University Libraries, Virginia Tech*. https://doi.org/10.7294/26860051.V2

Thomas, E. G., Shepherd, S. G., Kunduri, B. S. R., & Themens, D. R. (2024). Multi-frequency SuperDARN HF radar observations of the ionospheric response to the October 2023 annular solar eclipse. *Geophysical Research Letters*. https://doi.org/10.5281/zenodo.13742780.svg

Verhulst, T. G. W., & Stankov, S. M. (2020). Height dependency of solar eclipse effects: The ionospheric perspective. *Journal of Geophysical Research: Space Physics*, *125*(7), e2020JA028088. https://doi.org/10.1029/2020JA028088

Wang, W., Dang, T., Lei, J., Zhang, S., Zhang, B., & Burns, A. (2019). Physical processes driving the response of the F2 region ionosphere to the 21 August 2017 solar eclipse at millstone Hill. *Journal of Geophysical Research: Space Physics*, *124*(4), 2978–2991. https://doi.org/10.1029/2018JA025479

Watanabe, D., & Nishitani, N. (2013). Study of ionospheric disturbances during solar flare events using the SuperDARN Hokkaido radar. *Advances IN Polar Science*, *24*(1), 12. https://doi.org/10.3724/SP.J.1085.2013.00012

Weimer, D. R. (2005). Predicting surface geomagnetic variations using ionospheric electrodynamic models. *Journal of Geophysical Research*, *110*(A12). https://doi.org/10.1029/2005JA011270

Yau, A. W., Foss, V., Howarth, A. D., Perry, G. W., Watson, C., & Huba, J. (2018). Eclipse-induced changes to topside ion composition and field-aligned ion flows in the August 2017 solar eclipse: E-Pop observations. *Geophysical Research Letters*, *45*(20), 10829–10837. https://doi.org/10.1029/2018GL079269

Zhang, S.-R., Erickson, P. J., Goncharenko, L. P., Coster, A. J., Rideout, W., & Vierinen, J. (2017). Ionospheric bow waves and perturbations induced by the 21 August 2017 solar eclipse. *Geophysical Research Letters*, *44*(24), 12067–12073. https://doi.org/10.1002/2017GL076054